Fitting of random tessellation models to keratin filament networks

Michael Beil[1] **Stefanie Eckel**[2] **Frank Fleischer**[3]
Hendrik Schmidt[2] **Volker Schmidt**[2] **Paul Walther**[4]

9th December 2005

[1]Department of Internal Medicine I
University Hospital Ulm, D-89070 Ulm, Germany
Phone: +49 731 500 24860
Fax: +49 731 500 24302

[2]Department of Stochastics
University Ulm, D-89069 Ulm, Germany
Phone: +49 731 50 23531
Fax: +49 731 50 23649

[3]Department of Applied Information Processing & Department of Stochastics
University Ulm, D-89069 Ulm, Germany
Phone: +49 731 50 23617
Fax: +49 731 50 23649

[4]Electron Microscopy Facility
University Ulm, D-89069 Ulm, Germany
Phone: +49 731 50 23441
Fax: +49 731 50 23383

Corresponding author:
Frank Fleischer
Department of Applied Information Processing & Department of Stochastics
University Ulm, D-89069 Ulm, Germany
Phone: +49 731 50 23617
Fax: +49 731 50 23649
E-mail: frank.fleischer@uni-ulm.de

Abstract

The role of specific structural patterns in keratin filament networks for regulating biophysical properties of epithelial cells is poorly understood. This is at least partially due to a lack of methods for the analysis of filament network morphology. We have previously developed a statistical approach to the analysis of keratin filament networks imaged by scanning electron microscopy. The segmentation of images in this study resulted in graph structures, i.e. tessellations, whose structural characteristics are now further investigated by iteratively fitting geometrical statistical models. An optimal model as well as corresponding optimal parameters are detected from a given set of possible random tessellation models, i.e. Poisson-Line tessellations (PLT), Poisson-Voronoi tessellations (PVT) and Poisson-Delaunay tessellations (PDT). Using this method, we investigated the remodeling of keratin filament networks in pancreatic cancer cells in response to transforming growth factor α (TGFα), which is involved in pancreatic cancer progression. The results indicate that the fitting of random tessellation models represents a suitable method for the description of complex filament networks.

Keywords CYTOSKELETON; KERATIN; RANDOM TESSELLATIONS; SCANNING ELECTRON MICROSCOPY; STOCHASTIC GEOMETRY

1 Introduction

Keratins belong to the group of intermediate filament proteins and are expressed in epithelial cells (Herrmann and Aebi, 2004). Intermediate filaments can be distinguished from other filamentous systems of the cytoskeleton by their unique biochemical and biophysical properties (Fudge et al., 2003; Janmey et al., 1991; Zackroff and Goldmann, 1979). Thus, this filament system appears to play a specific role for defining the mechanical properties of cells (Wang and Stamenovic, 2000 and 2002). In fact, the importance of keratin filaments for the viscoelastic properties of epithelial cells was confirmed by single cell probing (Beil et al., 2003; Suresh et al., 2005). Dynamic changes of these mechanical properties are necessary for the migration of cancer cells during tissue invasion and metastasis (Kole et al., 2005; Wolf et al., 2003). These changes can be accomplished by modulating the keratin network architecture through multiple interactions between kinases, phosphatases and other regulatory proteins (Coulombe and Omary, 2002; Strnad et al., 2002). However, the knowledge about the processes defining the morphology of keratin networks is incomplete (Herrmann and Aebi, 2004). This is at least partially due to a lack of models for the description of complex networks of filament structures.

Simulation models of filament assembly and network build-up are a valuable source of information (Portet et al., 2003). The comparison of simulated networks with image data obtained from cells, however, could be compromised by the variability of cell morphology and random artefacts during specimen processing. Furthermore, random cytoskeletal rearrangements appear to be an integral part of cytoskeleton dynamics (Kodama et al., 2004; Kirschner and Mitchison, 1986; Odde and Buettner, 1998). These processes can be taken into account by fitting statistical models to image analysis data. Widely used geometrical statistical models for network structures are random tessellations (Okabe et al., 2000; Stoyan et al., 1995). Prominent examples are Poisson-Line tessellations (PLT), Poisson-Voronoi tessellations (PVT) and Poisson-Delaunay tessellations (PDT). All three models are based on Poisson point processes in the Euclidean space, for our purposes in the plane (see below). These basic tessellation models can be iterated, for example by nesting (Maier and Schmidt, 2003; Weiss and Nagel, 1999), that means each mesh of the tessellation is further tessellated independently. Thereby more complex stochastic-geometric structures can be realised. Such

tessellation models, basic and iterated ones, allow for the reduction of complex randomly behaving structural scenarios to models described by only a few parameters. This leads to further knowledge of characteristics of the network with respect to expected moments or even distributions of characteristics like the number of segments per unit area or the number of segments emanating from a typical node.

In a previous study, we analyzed the reorganisation of keratin networks in the subcortical region of pancreatic cancer cells in response to transforming growth factor α (TGFα) (Beil et al., 2005). This subcellular compartment has been identified as a location with a highly dynamic turn-over of keratin filaments (Windoffer et al., 2004). Since the periphery of cultured cells represents a quasi 2D structure, analysis procedures could be implemented for 2D images of filament networks. Scanning electron microscopy (SEM) was applied to image individual keratin filaments after a pre-fixation extraction procedure (Beil et al., 2003). After an automated segmentation of the filament network, statistical features of network morphology revealed an increase of keratin filament density and isotropy in response to TGFα. In another paper we introduced an optimization procedure that determines an optimal tessellation model for a given data set out of a choice of random tessellation models (Gloaguen et al., 2005). Now, in this new study, iterated tessellation models based on PVT, PDT and PLT models are fitted to the segmented keratin network structures. The results demonstrate that TGFα induces a fundamental remodeling of keratin networks in pancreatic cancer cells. Based on the selection of best fitted models we will present a hypothetical scenario for the structural organisation of keratin networks in quiescent and stimulated cancer cells.

2 Materials and methods

2.1 Experimental set-up

The procedures for cell culture, specimen preparation, scanning electron microscopy (SEM) and image analysis have been described in detail in Beil et al. (2005). Therefore only a short summary is given here.

Panc-1 human pancreatic cancer cells (American Type Culture Collection, Manassas, VA)

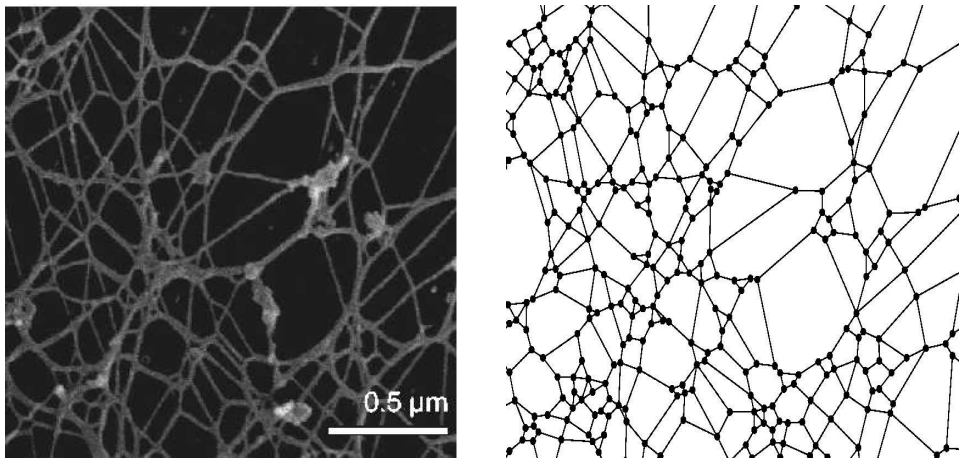

(a) Grayscale sample image (b) Corresponding graph structure

Figure 1: Image segmentation algorithm

were grown on glass chamber slides and incubated with 100 ng/ml TGFα (R&D Systems, Minneapolis, MN) for 30 min. Thereafter, non-keratin proteins were extracted from the cytoplasm of stimulated cells and untreated cells with a method partially based on a protocol by Svitkina and Borisy (1998). The specificity of this method for keratin filaments was previously demonstrated by immuno electron microscopy (Beil et al., 2003). After fixation with 4.0 % formaldehyde slides were gradually dehydrated and subjected to critical point drying. Samples were subsequently coated with 3 nm of platinum-carbon and imaged with a Hitachi S-5200 in-lens SEM (Tokyo, Japan). Sample regions at the periphery of cells were imaged with a 35000 x magnification (pixel size: 2.63 nm). The window size for a single sample was 1220×850 pixels ($\approx 3.22\ \mu m \times 2.44\ \mu m$). Altogether there were 15 Panc1 cells analyzed (7 cells after stimulation with TGFα and 8 untreated cells).

The original grayscale images were transformed into binary images by adaptive thresholding. After a preprocessing to reduce noise effects, the binary images were skeletonized using morphological thinning thereby preserving homotopy. The resulting skeletons were pruned and transformed into line segment structures. Finally, these line segment structures were modified by an adaptive merging of nearby crosspoints (Beil et al. 2005). For an illustration of the applied algorithm see Figure 1. The resulting line segment structures, i.e. graphs, were in the following analyzed with respect to different possible tessellation models describing them.

2.2 Model choice based on comparison of distance measures

In the present section we introduce the applied model choice algorithm. Further information about the model choice procedure including examples for simulated input data can be found in Gloaguen et al. (2005). Mathematical definitions of the used tessellation models are provided in the Appendix.

Characteristics of input data and unbiased estimation of global characteristics
With respect to the input data certain characteristics describing the spatial-geometric structure are estimated. In particular, we consider characteristics which are measured per unit area. This comprises the characteristics $\lambda_1, \ldots, \lambda_4$, which correspond to the mean number of vertices, the mean number of edges, the mean number of meshes, and the mean total length of edges, respectively, always with respect to the unit area.

The characteristics $\lambda_1, \ldots, \lambda_4$ can be interpreted as global characteristics and they are chosen both because they are a good representation of the underlying tessellation model and because of their relative simplicity regarding theoretical formulae; see Maier and Schmidt (2003) and Tables 1 and 6. It would also be possible to consider local characteristics which refer to single meshes, like the mean edge-length per mesh, the mean perimeter per mesh, and the mean area per mesh. However, it turned out that these characteristics are less useful, because unbiased estimators for them are not quite obvious. Therefore, in the following, we concentrate on the global characteristics and consider the vector

$$\lambda = (\lambda_1, \ldots, \lambda_4)^\top . \tag{2.1}$$

The intensities of the vector λ given by (2.1) have to be estimated from the graph structure that arises from the original SEM images. Hence, we need a vector of (intensity) estimators

$$\widehat{\lambda} = (\widehat{\lambda}_1, \ldots, \widehat{\lambda}_4)^\top , \tag{2.2}$$

where each entry of this vector is an estimator for the corresponding entry in (2.1). Further information about estimation of such characteristics can be found in e.g. Baddeley and

Jensen (2004) or Ohser and Mücklich (2000). In this paper we use the following estimators,

$$\widehat{\lambda} = \frac{1}{|W|} \left(n_v \, , n_e \, , n_c \, , l_e \, \right)^\top , \tag{2.3}$$

where $|W|$ denotes the area of thesampling window W. Obviously, with n_v denoting the number of vertices contained within W, the estimator $\widehat{\lambda}_1 = n_v/|W|$ is an unbiased estimator for λ_1. In order to get the unbiased estimator $\widehat{\lambda}_2 = n_e/|W|$ for λ_2, we consider the number n_e of edges whose lexicographically smaller end point is contained in W. Similarly, n_m denotes the number of meshes obtained by counting appropriately chosen associated points of the meshes, for example the lexicographically smallest vertice of each mesh which leads to the unbiased estimator $\widehat{\lambda}_3 = n_m/|W|$ for λ_3. Finally, l_e measures the total length of the edge-set contained in W and $\widehat{\lambda}_4 = l_e/|W|$ is an unbiased estimator for λ_4.

Distance measures

In order to compare the estimated vector of characteristics of the input data with the corresponding vector of calculated values for the tessellation models under comparison, different distance measures have to be considered.

Several possibilities for such distance measures can be examined. Particularly, if $x = (x_1, \ldots, x_n)^\top$ and $y = (y_1, \ldots, y_n)^\top$ denote two vectors with n entries, the following distance measures have been taken into account.

Euclidean distance

$$d_e(x,y) = \sqrt{\sum_{i=1}^{n} (x_i - y_i)^2} \quad \text{(absolute)} \qquad d'_e(x,y) = \sqrt{\sum_{i=1}^{n} \left(\frac{x_i - y_i}{x_i} \right)^2} \quad \text{(relative)}$$

, absolute value distance

$$d_a(x,y) = \sum_{i=1}^{n} |x_i - y_i| \quad \text{(absolute)} \qquad d'_a(x,y) = \sum_{i=1}^{n} \left| \frac{x_i - y_i}{x_i} \right| \quad \text{(relative)}$$

, maximum norm distance

$$d_m(x,y) = \max_{i=1,\ldots,n} |x_i - y_i| \quad \text{(absolute)} \qquad d'_m(x,y) = \max_{i=1,\ldots,n} \frac{|x_i - y_i|}{x_i} \qquad \text{(relative)}$$

.

Notice that absolute distance measures like d_e, d_a, and d_m can be strongly influenced by components with possibly extreme values, whereas relative measures like d'_e, d'_a, and d'_m should be preferable for our purposes since a certain effect of averaging occurs and since they are scale-invariant. Especially the scale-invariance is very useful because this means that the choice of the optimal model becomes independent from the scale on which the data is measured. So, (for example) in our case it does not matter if we compute on a scale of nm or in pixels. For absolute distance measures this is in general not true. Furthermore notice that the relative distance measures are not symmetric in their arguments x and y anymore. Therefore, it is necessary to handle distance measures of this kind with care in the subsequent examinations. This means that if we use a certain relative distance measure, the scaling always needs to be done with respect to the same reference argument. An observation we made is that for almost all investigated cases the result of the model choice was the same, no matter what type of relative distance measure was chosen. Additionally, optimal intensity values have been nearly identical. Therefore we focus in the following on one of the relative distance measures, namely the relative Euclidean distance measure, reflecting a very natural choice for a metric.

Non-iterated random tessellations

For a mathematical definition of a random tessellation see Appendix A.2. Figure 2 shows realizations of three basic non-iterated tessellation models, namely the PLT, the PVT, and the PDT. All three models were realised in such a way that the mean total length per unit area was the same for all three cases.

The PLT is induced by a random Poisson line process in $\mathbb{R}^2$ which can be interpreted as a Poisson point process on $\mathbb{R} \times [0, \pi]$. This is due to the fact that each line is determined by the signed perpendicular distance between the line and the origin o and by the angle measured in anti-clockwise direction between the orientation vector of the line and the x-axis. Generally, the parameter γ_{PLT} is interpreted as the mean total length of edges per unit area.

The meshes of a (deterministic) Voronoi tessellation are convex polygons in $\mathbb{R}^2$, namely the closure of all planar points which are closest (in the sense of the 2-dimensional Euclidean

metric) to the nucleus of this mesh. If the set of nuclei is induced by a stationary random Poisson point process in $\mathbb{R}^2$, we call the resulting tessellation a (random) PVT. The parameter γ_{PVT} of the PVT corresponds to the intensity of its generating Poisson point process and can be interpreted as the mean number of meshes per unit area.

The PDT is closely related to the PVT. Indeed, consider a PVT, i.e., a Voronoi tessellation whose nuclei are induced by a stationary Poisson point process. The meshes of its corresponding PDT are obtained by connecting the nuclei of neighboring meshes, i.e., meshes that share a common edge, of the PVT. Since in the case of a PVT the nuclei are not collinear with probability one, i.e., almost surely three pairwise different points do not lie on the same line, the meshes of the corresponding PDT are triangles. The intensity γ_{PDT} can be interpreted as the mean number of vertices of the PDT per unit area.

Table 1 shows the relationship between the four intensities $\lambda_1, ..., \lambda_4$ and a (basic) tessellation with parameter γ; see e.g. Stoyan et al. (1995). Hence, in each case γ has to be interpreted differently.

Table 1: Values of $\lambda_1, \ldots, \lambda_4$ for a given tessellation with parameter γ

Tessellation	λ_1	λ_2	λ_3	λ_4
PLT	$\frac{1}{\pi}\gamma^2$	$\frac{2}{\pi}\gamma^2$	$\frac{1}{\pi}\gamma^2$	γ
PVT	2γ	3γ	γ	$2\sqrt{\gamma}$
PDT	γ	3γ	2γ	$\frac{32}{3\pi}\sqrt{\gamma}$

Iterated random tessellations

Non-iterated tessellations can be used to construct more sophisticated tessellation models called iterated tessellations. This means that each mesh of some initial tessellation is further tessellated using a certain tessellation model, which is not necessarily the same model as in the case of the initial tessellation. An iterated random tessellation X can itself be an initial tessellation for a further tessellation. In particular, it is possible to construct random tessellations with $k \geq 2$ iterations which are called k-fold iterated tessellations. For example, a X_0/X_1 tessellation denotes a 1-fold iterated tessellation, which can be described by the two corresponding parameters γ_0 and γ_1, respectively. Trivially, each non-iterated tessellation can be regarded as a 0-fold iterated tessellation. In the case of 1-fold iterated tessellations, if both for X_0 and X_1 PLTs, PVTs, or PDTs are considered, we end up with

nine possible models; see Figure 3. The so-called Bernoulli thinning allows for variants of k-fold tessellations. There the parameter p is the probability for an initial mesh to be iterated by the component tessellation. Figure 4 displays realizations of 1-fold nestings, where the Bernoulli thinning technique has been applied in the case of a $X_0/p\,X_1$-nesting ($p = 0.75$). For a mathematical definition of an iterated random tessellation as well as for mean value formulae see Appendix A.3

Optimal model choice

In this section we describe how an optimal tessellation model (and an optimal vector of corresponding intensities) is obtained. In particular, we consider tessellations consisting of an initial tessellation X_0 and a component tessellation X_1, as described above, where PLT, PVT, and PDT (see Figure 2) are considered as models both for X_0 and X_1 leading to 9 different possible model choices. Each of these iterated tessellations can be described by three parameters, the parameters $\gamma_0 > 0$ and $\gamma_1 > 0$ for X_0 and X_1, respectively and the probability $1-p$ of the Bernoulli-thinning. Figure 3 displays realizations of all iterated models considered, while Figure 4 illustrates realizations of models where the thinning parameter p is less than one. For the sake of illustration, parameters in Figure 3 were chosen such that the mean total length of the segments per unit area is equal for each model and that the ratio between the mean total length of segments belonging to the initial tessellation and the mean total length of segments belonging to the component tessellation is equal to 0.5. Notice that the parameter γ for the three different basic models (PLT, PVT and PDT) has different meanings, but can be scaled by the usage of the formulae given in Table 1 in order to get comparable values, for example the total length per unit area. In order to obtain an optimal model choice together with corresponding parameters for the chosen model, first for each possible model separately, an optimal vector of parameters is determined. This is achieved by constructing a relative distance function $f_{model}(\gamma_0, \gamma_1, p)$ and by minimizing it for the given range of p, which usually is determined beforehand using prior knowledge about the system. If no knowledge is available, it is also possible to go through a range from 0 to 1 which is the maximal range for p. Therefore, by applying the relative Euclidean distance

measure, we obtain a relative distance function given by

$$f_{model}(\gamma_0, \gamma_1, p) = \sqrt{\sum_{i=1}^{4} \left(\frac{\widehat{\lambda}_i - \lambda_i^{model}}{\widehat{\lambda}_i} \right)^2}, \tag{2.4}$$

where $\widehat{\lambda}_i$ is the estimator for the i-th characteristic (see Eq. (2.3)) and λ_i^{model} is the theoretical mean value of the i-th characteristic with respect to the chosen model and the parameters γ_0, γ_1 and p. The formulae for the mean values of the four characteristics with respect to the nine different models can be found in Table 6 in the Appendix. After the determination of an optimal parameter vector, that means a parameter vector that minimizes the relative distance function, for each possible model separately, the corresponding relative distance values are compared. The model with the smallest optimal relative distance value is considered to be the optimal model of the models regarded. To summarize the model choice algorithm used, if we consider a pool of possible models $\{M_1, ..., M_n\}$, we first estimate the vector of characteristics $(\widehat{\lambda}_1, \widehat{\lambda}_2, \widehat{\lambda}_3, \widehat{\lambda}_4)$. Then for each model M_i, where $i = 1, ..., n$, the relative Euclidean distance $f_{M_i}(\gamma_0, \gamma_1, p)$ is minimized to get an optimal value $f_{M_i}^*$. Finally, the model M^* is considered to be optimal among all the models $M_1, ..., M_n$, where $M^* = argmin_{\{M_1,...,M_n\}} f_{M_i}^*$.

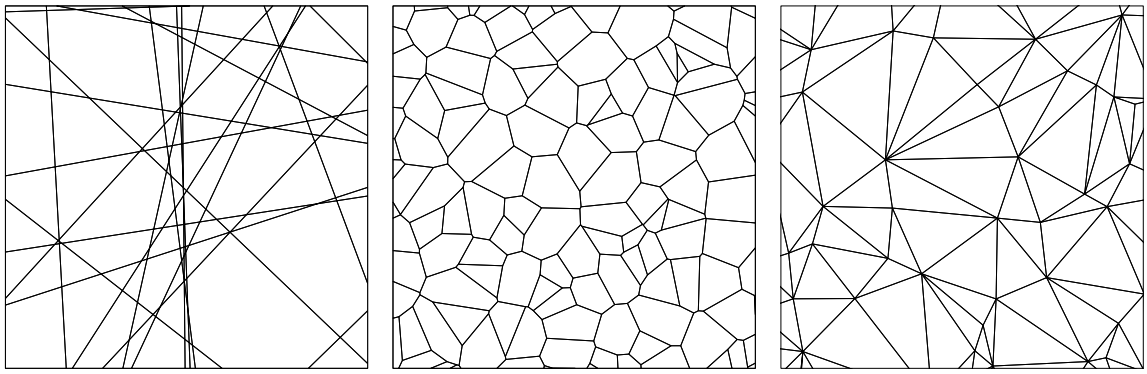

(a) PLT, $\gamma_{PLT} = 0.02$ (b) PVT, $\gamma_{PVT} = 0.0001$ (c) PDT, $\gamma_{PDT} = 0.000037$

Figure 2: Realizations of basic tessellations with parameter γ

Possible models considered

As it was mentioned before, we focus our investigations on models consisting of a an initial tessellation and a (embedded) component tessellation, where for both tessellation levels we choose between PDT, PVT, or PLT. These models cover a broad spectrum of cytoskeletal scenarios ranging from sets of long filaments whose shape is independent of crossings (PLT)

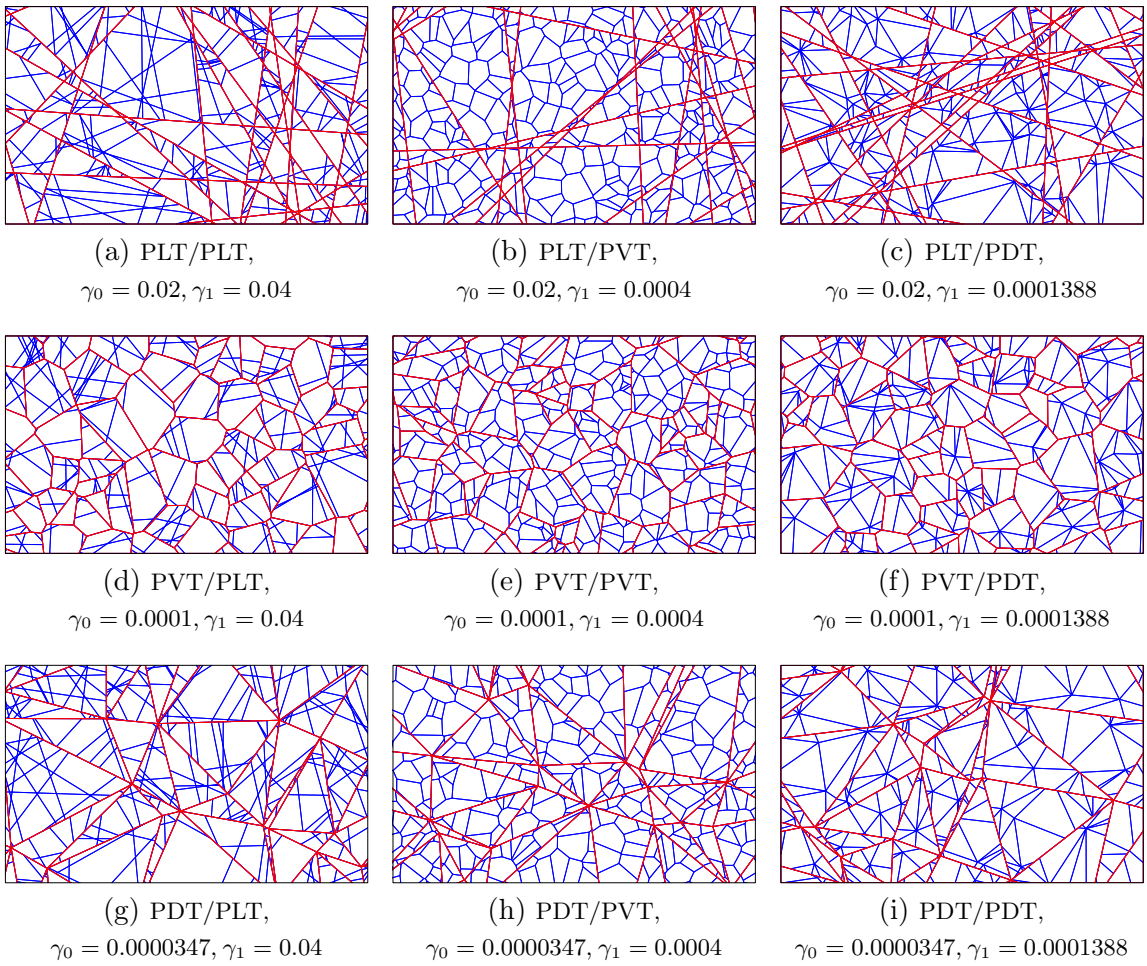

(a) PLT/PLT, $\gamma_0 = 0.02, \gamma_1 = 0.04$ (b) PLT/PVT, $\gamma_0 = 0.02, \gamma_1 = 0.0004$ (c) PLT/PDT, $\gamma_0 = 0.02, \gamma_1 = 0.0001388$

(d) PVT/PLT, $\gamma_0 = 0.0001, \gamma_1 = 0.04$ (e) PVT/PVT, $\gamma_0 = 0.0001, \gamma_1 = 0.0004$ (f) PVT/PDT, $\gamma_0 = 0.0001, \gamma_1 = 0.0001388$

(g) PDT/PLT, $\gamma_0 = 0.0000347, \gamma_1 = 0.04$ (h) PDT/PVT, $\gamma_0 = 0.0000347, \gamma_1 = 0.0004$ (i) PDT/PDT, $\gamma_0 = 0.0000347, \gamma_1 = 0.0001388$

Figure 3: Realizations of possible iterated tessellations with parameters γ_0 and γ_1

to networks composed of branched filaments (PVT, PDT). The latter type of networks can further be classified with respect to the branching points. The branching in the PVT model mostly reflects the division of a filament into two, whereas the branching points in the PDT model represent organization centers giving rise to more than two filaments. Notice that in principle, the model choice algorithm proposed is not restricted to these models, but can easily be extended to other models, as long as mean values for these models are available, either by an analytical formulae or by simulation. The three basic models we use seem to be a good choice, since on the one hand, if regarded separately, they are of a certain simplicity, but on the other hand, especially if iterated models are regarded, they can cover a wide range of different network structures. This variety is broadened even more by the introduction of a Bernoulli thinning parameter p being the probability for a mesh of the intitial tessellation to be further tessellated by a component tessellation. For further investigations we restricted

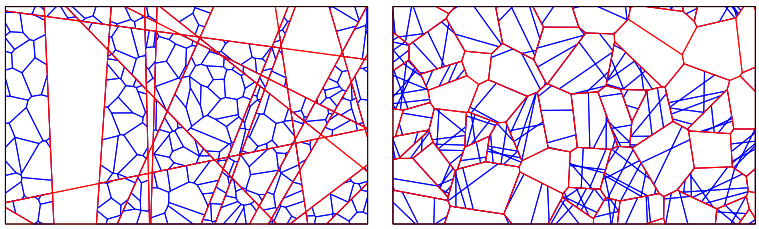

(a) PLT/PVT, $\gamma_0 = 0.02, \gamma_1 = 0.0004, p = 0.75$

(b) PVT/PLT, $\gamma_0 = 0.0001, \gamma_1 = 0.04, p = 0.75$

Figure 4: Realizations of iterated tessellations with Bernoulli thinning

the parameter p to a range from 0.9 to 1 thereby reflecting the small probability $1 - p$ that a non-iteration might happen for an initial mesh, e.g. due to the occurence of intracellular vacuoles. In order to clarify the question how many iteration levels should be used, investigations were performed with smaller cutouts of the samples. These investigations led to the observation that for non-iterated, i.e. basic tessellations, the relative distance values are very similar for cutouts compared to whole sampling windows. For one-fold iterated models, the relative distance values significantly improve if sampling windows are regarded compared to relative distance values for smaller cutouts. These observations lead to the assumption that iterated models might be preferable compared to non-iterated tessellations with respect to the sample sizes regarded. Also from a biological viewpoint, an iterated model might be a better choice compared to a non-iterated tessellation, since it allows to reflect more precisely the complex procedures in the keratin filament network. On the other hand it does not seem very reasonable to take into account more complex models than those having two tessellation levels. More than two tessellation levels might be possible from a theoretical point of view, but especially with respect to the observed sampling sizes, a third level seems to be almost impossible to detect. Additionally an improvement in the optimal distance value seems thereby hard to achieve.

Individual samples vs. mean values

Apart from regarding single samples, it is useful to investigate mean samples in the sense that a vector of characteristics $(\bar{\widehat{\lambda}}_1, \bar{\widehat{\lambda}}_2, \bar{\widehat{\lambda}}_3, \bar{\widehat{\lambda}}_4)$ is estimated, where

$$\bar{\widehat{\lambda}}_i = \frac{1}{n} \sum_{j=1}^{n} \widehat{\lambda}_{ij} \tag{2.5}$$

and $\widehat{\lambda}_{ij}$ is the estimated i-th characteristic for the j-th sample ($1 \leq i \leq 4$; $1 \leq j \leq n$). Notice that this is a reasonable method since the samples of an individual group can be considered to be independent and identically distributed. Such a procedure is comparable to a situation, where data is available for a much larger sampling window.

2.3 Software aspects

The software developed and used for image analysis as well as for the model fitting procedure is included in the GeoStoch library system. GeoStoch is a Java-based open-library system developed by the Department of Applied Information Processing and the Department of Stochastics of the University of Ulm. This system can be used for stochastic-geometric modelling and spatial statistical analysis of image data (Mayer, 2003; Mayer et al., 2004; http://www.geostoch.de).

3 Results

The filament networks as segmented in Beil et al. (2005) were subjected to a model fitting procedure. As a first step the vectors of mean values for the four characteristics of the network structures have been regarded. Remember that the investigation of these mean vectors is similar to the investigation of single samples observed through a larger sampling window. Results for the fitting procedure for the vectors of mean values are presented in Section 3.1. In order to obtain more specific results, each sample image was also analyzed separately. Results of the individual fitting procedure can be found in Secion 3.2.

3.1 Model fitting for the vectors of mean characteristics

Results for the model choice procedure with respect to mean values for each of the two groups are displayed in Tables 2 and 3. The relative Euclidean distance was used, but results do not vary much if other relative distance measures are regarded. For the group of untreated cells it is visible that the favored model is that of a PVT/PLT, in other words the PVT/PLT model has a minimal distance value, while for the group of cells stimulated with TGFα the optimal model is that of a PDT/PLT. Notice that the values of the parameter

Table 2: Optimal parameter choices for possible models concerning mean values for the group of untreated cells

Model	Distance	γ_0	γ_1	p
One-fold iterations				
PLT/PLT	0.0057	0.022031	0.025125	0.9
PLT/PVT	0.0205	0.031608	0.000057	0.9
PLT/PDT	0.0560	0.029103	0.000033	0.9
PVT/PLT	**0.0015**	0.000049	0.033860	0.9
PVT/PVT	0.2023	0.000298	0.000030	1.0
PVT/PDT	0.1054	0.000101	0.000083	0.9
PDT/PLT	0.0447	0.000026	0.0331583	0.9
PDT/PVT	0.1123	0.000067	0.000123	0.9
PDT/PDT	0.1477	0.000053	0.000070	0.9
Basic tessellations				
PLT	0.2994	0.048714	-	-
PVT	0.2077	0.000539	-	-
PDT	0.8492	0.000362	-	-

p differ only slightly between the two optimal models for the two different groups (0.9 vs. 0.915). Figure 5 shows, for the sake of illustration, segmented graph structures of both groups together with sample realizations of the optimal model for the vector of mean characteristics of each group. Obviously, the similarity between these pictures can not be perfect, since there exists a variability between different realizations of the same model. Notice also that a comparison between the optimal iterated model and the optimal basic model, i.e. the model that has minimal distance out of PVT, PLT and PDT, yields a large improvement considering the quality of approximation (Tables 2 and 3).

3.2 Model fitting for single samples

In order to get a more specific interpretation of the results for the mean values of characteristics, optimal models have been determined separately for each individual sample. From the results displayed in Tables 4 and 5 it can be deduced that in the case of untreated cells a quite clear decision for the PVT/PLT is made in all cases meaning that always the

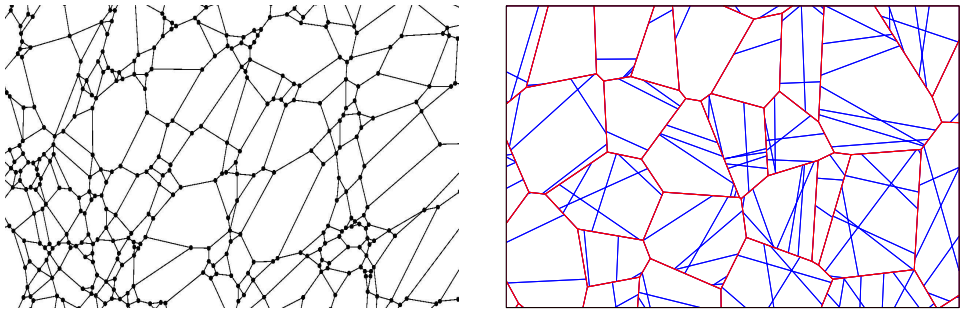

a) Segmented graph structure and sample realization of optimal PVT/PLT model for the group of untreated cells

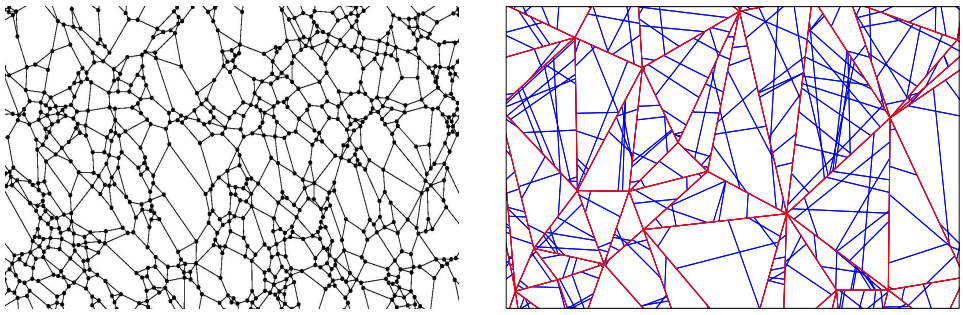

b) Segmented graph structure and sample realization of optimal PDT/PLT model for the group of cells stimulated with TGFα

Figure 5: Comparison between segmented image data and realizations of optimal model for both groups

Table 3: Optimal parameter choices for possible models concerning mean values for the group of cells stimulated with TGFα

Model	Distance	γ_0	γ_1	p
One-fold iterations				
PLT/PLT	0.0084	0.040824	0.018099	1.0
PLT/PVT	0.0024	0.044430	0.000054	1.0
PLT/PDT	0.0129	0.040115	0.000042	0.9
PVT/PLT	0.0024	0.044430	0.000054	1.0
PVT/PVT	0.2311	0.000835	0.000000	1.0
PVT/PDT	0.0911	0.000131	0.000177	0.9
PDT/PLT	**0.0005**	0.000038	0.041888	0.915
PDT/PVT	0.1030	0.000145	0.000160	0.9
PDT/PDT	0.1068	0.000087	0.000121	0.9
Basic tessellations				
PLT	0.2605	0.063116	-	-
PVT	0.2312	0.000827	-	-
PDT	0.8103	0.000622	-	-

PVT/PLT is considered as an optimal model. Notice that in some cases dual solutions for the optimal model are possible due to symmetries in the corresponding formulae, especially in the case $p = 1$. With regard to the group of cells stimulated with TGFα a different decision is viewable, meaning that for three samples, as well as for the mean characteristics, the decision is at least partially in favor of a PDT/PLT as an optimal model, while the other four samples lead to a decision in favor of a PVT/PLT. For both groups as well as for all individual cells, a model of branched filaments (PVT or PDT) was determined as best fit for the first iteration in contrast to an interaction-free model (PLT), thus emphasizing the characteristics of the keratin cytoskeleton as a branched filament network.

4 Discussion

The rules governing the dynamic modulation of keratin network architecture remain to be elucidated (Herrman and Aebi, 2004). Major studies were based on single filament tracking (e.g. Windoffer et al., 2004). Global parameters of filament networks can be analyzed by

Table 4: Optimal models for individual samples of the group of untreated cells

sample	optimal model	distance
1	PVT/PLT	0.0325
2	PVT/PLT	0.0011
3	PVT/PLT or PLT/PLT	0.0019
4	PVT/PLT	0.0079
5	PVT/PLT or PLT/PVT	0.0161
6	PVT/PLT	0.0274
7	PVT/PLT	0.0071
8	PVT/PLT or PLT/PVT	0.0066

Table 5: Optimal models for individual samples of the group of cells stimulated with TGFα

sample	optimal model	distance
1	PDT/PLT or PLT/PDT	0.0104
2	PDT/PLT	0.0146
3	PDT/PLT or PLT/PDT	0.0138
4	PVT/PLT or PLT/PLT	0.0040
5	PVT/PLT	0.0044
6	PVT/PLT or PLT/PLT	0.0026
7	PVT/PLT or PLT/PVT	0.0050

statistical image analysis. In previous studies, we implemented such methods to determine morphological features of keratin networks such as filament density and isotropy (Beil et al., 2005; Portet et al., 1999; Vassy et al., 1996). However, these investigations also revealed a certain degree of heterogeneity in supposedly homogeneous cell populations. Technical as well as biological reasons may contribute to this heterogeneity. An analysis based on fitting statistical models to real image data considers these facts and, moreover, focuses on relevant and complex features of network architecture. In this study, we take into account one-fold iterated tessellations that are composed of PVT, PDT and PLT as choices for both the initial and the component tessellation. Thereby it is possible to model complicated structures and also a wide range of spatial structures using models that can be described by only a few parameters. Although these models are stationary and isotropic with respect to the plane, if a fixed and not too large sampling window is regarded, they allow a large variability with respect to instationarities and anisotropies that can occur in data samples. Differently worded, realizations of the models considered in a fixed sampling window can look quite anisotropic and instationary even though the models themselves are isotropic and stationary. This is in accordance to the observations made in our previous study (Beil et al., 2005).

The fitting of geometrical statistical models (iterated tessellations based on PVT, PDT and PLT) to keratin filament networks demonstrates that TGFα induces a distinct remodeling of network architecture at the cell periphery of pancreatic cancer cells. TGFα has been shown to induce activation of intracellular signaling pathways in these cells (Seufferlein et al., 1999) resulting in keratin phosphorylation (Omary et al., 1998) which could lead to filament network reorganisation (Coulombe and Omary, 2002). Since keratin networks regulate cellular viscoelasticity and motility in epithelial cells (Beil et al., 2003), the findings of this study support a role of TGFα for the migration of cancer cells. In fact, TGFα has been shown to promote pancreatic cancer progression (Wagner et al., 2001) which requires migration of transformed cells (Ellenrieder et al., 1999).

The results of the model fitting revealed important structural details of keratin networks in pancreatic cancer cells. The PVT/PLT model was selected as an optimal model for all sample regions from untreated cancer cells. In TGFα - stimulated cancer cells, no uniform

model could be selected. However, all sample regions could be modeled either by a PDT/PLT or a PVT/PLT model with the PDT/PLT model being the best fit with respect to overall mean values. Since the PVT/PLT model is found to be a best fit for unstimulated cells, the TGFα - stimulated cells with this model are probably still in transition with the keratin network changes proceeding slower than in the other cells after stimulation with TGFα.

How can these findings be interpreted in the context of keratin function which is to provide epithelial cells with the ability to sustain mechanical stress (Coulombe and Omary, 2002). The major difference between the keratin network model of untreated and TGFα - stimulated pancreatic cancer cells is the model of the basic tessellation. The PVT model for unstimulated cells (Figure 2b) suggests a quiescent state with a certain degree of functional isotropy. In contrast, TGFα induces a network reorganisation (PDT, Figure 2c) which leads to filament arrangements in a few preferred directions in parallel with the build-up of major branching points. This way, the cancer cell can regulate the response to mechnical stress, such as the remodeling of the cytoplasm during migration. Our recent finding that the keratin filaments in untreated pancreatic cancer cells are more uniformly oriented than the filaments of TGFα - treated cells (Beil et al., 2005) is in accordance with these data.

The PLT model is found to be a best fit for the embedded tessellation for both groups of cancer cells leading to the hypothesis that cancer cells tend to stabilize the primary tessellation mesh (PVT or PDT) by internal cross-beams. Importantly, no combination of PDT and PVT models, i.e. PVT/PVT, PDT/PDT, PVT/PDT or PDT/PVT, is found as a best fit for neither group, thus, further supporting this hypothesis. The significant improvement of the quality of approximation by one-fold iterations in contrast to basic tessellations (Tables 2 and 3) strongly suggests that this principle of network architecture is a realistic scenario. On the other hand, apart from the fact that a mathematical treatment of these models becomes more and more complicated, two-fold or even three-fold scenarios do not seem to be a realistic assumption. They might only be reasonable choices if very long filaments could be observed. As it is shown in Beil et al. (2005), this is not the case for the data in our study.

Although it is well understood that the role of keratin networks as dynamic scaffolds can be fulfilled by modulating the network architecture (Coulombe and Wong, 2004), the relation-

ship between specific structural patterns of keratin networks and biomechanical properties of entire cells or subcellular compartments remain to be defined. Keratin networks function as a dynamic scaffold in epithelial cells and are the dominant cytoskeletal system for the regulation of viscoelastic properties, for example, during cell migration (Coulombe and Wong, 2004). Simulation models revealed that the crosslink density is an important feature for the regulation of the macroscopic response of cytoskeletal networks (Head et al., 2003). The approach presented in this study provides the opportunity to estimate biophysical properties of keratin networks and cells based on models derived from real image data. Thereafter, these estimations can be verified by probing cytoskeletal networks or entire cells (Keller et al., 2003; Suresh et al., 2005). Importantly, the keratin network is not an isolated filament system which function separately from other filament assemblies of the cytoskeleton or from other subcellular compartments. Thus, the findings of this study can only reflect the structural and functional aspects of keratin networks in a limited way. However, model systems, such as tensegrity (Ingber, 2003), which consider the filamentous cytoskeleton as an integrated system emphasized the important role of keratin intermediate filaments for defining mechanical properties of cells (Wang and Stamenovic, 2000).

In conclusion, we have analyzed the architecture of keratin filament networks by fitting geometrical statistical models. The findings of this study indicate that the growth factor TGFα induces profound changes of the keratin filament network in pancreatic cancer cells demonstrating that this approach can provide important insights into the processes governing network morphology. Further research into the relationship between local and global features of keratin network architecture and biophysical properties could contribute to the understanding of fundamental biological processes such as cell migration.

Acknowledgements

We thank Elke Wolff-Hieber and Eberhard Schmid for expert technical assistance. We would also like to thank the reviewers for valuable comments and suggestions. This project was partly supported by the Deutsche Forschungsgemeinschaft (SFB 518). Stefanie Eckel is supported by a grant of the graduate college 1100 at the University of Ulm.

References

[1] Baddeley A. J., Vedel Jensen E. B., 2004. Stereology for Statisticians. Chapman & Hall.

[2] Beil M., Braxmeier H., Fleischer F., Schmidt V., Walther P., 2005. Quantitative analysis of keratin filament networks in scanning eletron microsopy images of cancer cells. J Microsc. 220, 84-95.

[3] Beil M., Micoulet A., von Wichert G., Paschke S., Walther P., Omary M. B., Van Veldhoven P. P., Gern U., Wolff-Hieber E., Eggermann J., Waltenberger J., Adler G., Spatz J., Seufferlein T., 2003. Sphingosylphosphorylcholine regulates keratin network architecture and visco-elastic properties of human cancer cells. Nat Cell Biol. 5, 803-11.

[4] Coulombe P. A., Omary M. B., 2002. 'Hard' and 'soft' principles defining the structure, function and regulation of keratin intermediate filaments. Curr Opin Cell Biol. 14, 110-22.

[5] Coulombe P. A., Wong P., 2004. Cytoplasmic intermediate filaments revealed as dynamic and multipurpose scaffolds. Nat Cell Biol. 6, 699-706.

[6] Ellenrieder V., Adler G., Gress T. M., 1999. Invasion and metastasis in pancreatic cancer. Ann Oncol. 10, 46-50.

[7] Fudge D. S., Gardner K. H., Forsyth V. T., Riekel C., Gosline J. M., 2003. The mechanical properties of hydrated intermediate filaments: insights from hagfish slime threads. Biophys J. 85, 2015-27.

[8] Gloaguen C., Fleischer F., Schmidt H., Schmidt V., 2005. Fitting of stochastic telecommunication network models, via distance measures and Monte-Carlo tests. Telecommunication Systems (in press).

[9] Head D. A., Levine A. J., MacKintosh F. C. (2003). Deformation of crosslinked semiflexible polymer networks. Phys Rev Let. 91, 108102.

[10] Herrmann H., Aebi U. (2004). Intermediate filaments: molecular structure, assembly mechanism, and integration into functionally distinct intracellular Scaffolds. Annu Rev Biochem. 73, 749-89.

[11] Ingber D. E. (2003). Tensegrity I: Cell structure and hierarchical systems biology. J Cell Sci. 116, 1157-73.

[12] Janmey P. A., Euteneuer U., Traub P., Schliwa M. (1991). Viscoelastic properties of vimentin compared with other filamentous biopolymer networks. J Cell Biol. 113, 155-60.

[13] Keller M., Tharmann R., Dichtl M. A., Bausch A. R., Sackmann E. (2003). Slow filament dynamics and viscoelasticity in entangled and active actin networks. Philos Transact A Math Phys Eng Sci. 361, 699-711.

[14] Kirschner M., Mitchison T. (1986). Beyond self assembly: from microtubules to morphogenesis. Cell. 45, 329-42.

[15] Kodama A., Lechler T., Fuchs E., (2004). Coordinating cytoskeletal tracks to polarize cellular movements. J Cell Biol. 167, 203-7.

[16] Kole T. P., Tseng Y., Jiang I., Katz J. L., Wirtz D. (2005). Intracellular mechanics of migrating fibroblasts. Mol Biol Cell. 16, 328-38.

[17] Maier R., Schmidt V. (2003). Stationary iterated tessellations. Advances in Applied Probability. 35, 337-53.

[18] Mayer J., (2003). On quality improvement of scientific software: Theory, methods, and application in the GeoStoch Development. Doctoral Dissertation, University of Ulm.

[19] Mayer J., Schmidt V., Schweiggert F., (2004). A unified simulation framework for spatial stochastic models. Simulation Modelling Practice and Theory. 12, 307-26.

[20] Møller J., (1989). Random tessellations in $\mathbb{R}^d$. Advances in Applied Probability. 21, 37-73.

[21] Odde D. J., Buettner H. M. (1998). Autocorrelation function and power spectrum of two-state random processes used in neurite guidance. Biophys. Journal 75, 1189-96.

[22] Ohser J., Mücklich F., (2000). Statistical Analysis of Microstructures in Materials Science. J.Wiley & Sons, Chichester.

[23] Okabe A., Boots B., Sugihara K., Chiu S. N., (2000). Spatial Tessellations. 2nd ed., J.Wiley & Sons, Chichester.

[24] Omary M. B., Ku N. O., Liao J., Price D., (1998). Keratin modifications and solubility properties in epithelial cells and in vitro. Subcellular Biochem. 31, 105-40.

[25] Portet S., Vassy J., Beil M., Millot G., Hebbache A., Rigaut J. P., Schoevaert D. (1999). Quantitative analysis of cytokeratin network topology in the MCF7 cell line. Cytometry. 35, 203-13.

[26] Portet S., Arino O., Vassy J., Schoevaert D., (2003). Organization of the cytokeratin network in an epithelial cell. J Theor Biol. 223, 313-33.

[27] Schneider R., Weil W., (2000). Stochastische Geometrie. Teubner, Stuttgart.

[28] Seufferlein T., Van Lint J., Liptay S., Adler G., Schmid R. M., (1999) Transforming growth factor alpha activates Ha-Ras in human pancreatic cancer cells with Ki-ras mutations. Gastroenterology. 116, 1441-52.

[29] Stoyan D., Kendall W. S., Mecke J., (1995). Stochastic Geometry and its Applications. J. Wiley & Sons, Chichester.

[30] Strnad P., Windoffer R., Leube R. E., (2002). Induction of rapid and reversible cytokeratin filament network remodeling by inhibition of tyrosine phosphatases. J Cell Sci. 115, 4133-48.

[31] Suresh S., Spatz J., Mills J. P., Micoulet A., Dao M., Lim C. T., Beil M., Seufferlein T., (2005) Connections between single-cell biomechanics and human disease states: gastrointestinal cancer and malaria. Acta Biomaterial. 1, 15-30.

[32] Svitkina T. M., Borisy G. G., (1998). Correlative light and electron microscopy of the cytoskeleton of cultured cells. Methods Enzymol. 298, 570-92.

[33] Vassy J., Beil M., Irinopoulou T., Rigaut J. P., (1996). Quantitative image analysis of cytokeratin filament distribution during fetal rat liver development. Hepatology. 23, 630-8.

[34] Wagner M., Greten F. R., Weber C. K., Koschnick S., Mattfeldt T., Deppert W., Kern H., Adler G., Schmid R. M., (2001). A murine tumor progression model for pancreatic cancer recapitulating the genetic alterations of the human disease. Genes Dev. 15, 286-93.

[35] Wang N., Stamenovic D., (2000). Contribution of intermediate filaments to cell stiffness, stiffening, and growth. Am J Physiol Cell Physiol. 279, C188-94.

[36] Wang N., Stamenovic D., (2002). Mechanics of vimentin intermediate filaments. J Muscle Res Cell Motil. 23, 535-40.

[37] Weiss V., Nagel W., (1999). Interdependencies of directional quantities of planar tessellations. Advances in Applied Probability 31, 664-78

[38] Windoffer R., Woll S., Strnad P., Leube R. E., (2004). Identification of novel principles of keratin filament network turnover in living cells. Mol Biol Cell. 15, 2436-48.

[39] Wolf K., Mazo I., Leung H., Engelke K., von Adrian U. H., Deryugina E. I., Strongin A. Y., Brocker E. B., Friedl P. (2003). Compensation mechanism in tumor cell migration: mesenchymal-ameoboid transition after blocking of pericellular proteolysis. Journal Cell Biology 160, 267-77.

[40] Zackroff R. V., Goldman R. D., (1979). In vitro assembly of intermediate filaments from baby hamster kidney (BHK-21) cells. Proc Natl Acad Sci USA. 76, 6226-30.

A Random Tessellations

For a detailed discussion of the mathematical background, we refer to Schneider and Weil (2000) and Stoyan et al. (1995). Further information about random (iterated) tessellations can also be found in Maier and Schmidt (2003), Møller (1989) and Okabe et al. (2000).

A.1 Basic notations

The abbreviations int $B, \partial B$, and B^c are used to denote the interior, the boundary, and the complement of a set $B \subset \mathbb{R}^2$, respectively, where $\mathbb{R}^2$ denotes the 2-dimensional Euclidean

space. Notice that by $|B|$ we denote the 2-dimensional Lebesgue measure for an arbitrary measurable set $B \in \mathbb{R}^2$, i.e. $|B|$ is the area of B.

The families of all closed sets, compact sets, and convex bodies (compact and convex sets) in $\mathbb{R}^2$ are denoted by $\mathcal{F}$, $\mathcal{K}$, and $\mathcal{C}$, respectively. Recall that a random closed set Ξ in $\mathbb{R}^2$ is a measurable mapping $\Xi : \Omega \to \mathcal{F}$ from some probability space $(\Omega, \mathcal{A}, \mathbb{P})$ into the measurable space $(\mathcal{F}, \mathcal{B}(\mathcal{F}))$, where $\mathcal{B}(\mathcal{F})$ denotes the smallest σ-algebra of subsets of $\mathcal{F}$ that contains all sets $\{F \in \mathcal{F}, F \cap K \neq \emptyset\}$ for any $K \in \mathcal{K}$. Particularly, the random closed set Ξ is called a random compact set or a random convex body if $\mathbb{P}(\Xi \in \mathcal{K}) = 1$ or $\mathbb{P}(\Xi \in \mathcal{C}) = 1$, respectively.

A.2 Random tessellations

A *tessellation* in $\mathbb{R}^2$ is a countable family $\tau = \{C_n\}_{n\geq 1}$ of convex bodies $C_n \in \mathcal{C}$ such that $\operatorname{int} C_n \neq \emptyset$ for all n, $\operatorname{int} C_n \cap \operatorname{int} C_m = \emptyset$ for all $n \neq m$, $\bigcup_{n\geq 1} C_n = \mathbb{R}^2$, and $\sum_{n\geq 1} \mathbb{1}_{\{C_n \cap K \neq \emptyset\}} < \infty$ for any $K \in \mathcal{K}$. Notice that the sets C_n, called the *meshes* of τ, are polygons in $\mathbb{R}^2$. The family of all tessellations in $\mathbb{R}^d$ is denoted by $\mathcal{T}$. A *random tessellation* $\{\Xi_n\}_{n\geq 1}$ in $\mathbb{R}^d$ is a sequence of random convex bodies Ξ_n such that $\mathbb{P}(\{\Xi_n\}_{n\geq 1} \in \mathcal{T}) = 1$. Notice that a random tessellation $\{\Xi_n\}_{n\geq 1}$ can also be considered as a marked point process $\sum_{n\geq 1} \delta_{[\alpha(\Xi_n), \Xi_n^0]}$, where $\alpha : \mathcal{C}' \to \mathbb{R}^d$, $\mathcal{C}' = \mathcal{C} \setminus \{\emptyset\}$, is a measurable mapping such that $\alpha(C) \in C$ and $\alpha(C + x) = \alpha(C) + x$ for any $C \in \mathcal{C}'$ and $x \in \mathbb{R}^d$, and where $\Xi_n^0 = \Xi_n - \alpha(\Xi_n)$ is the centered mesh corresponding to Ξ_n which contains the origin. The point $\alpha(C) \in \mathbb{R}^d$ is called the associated point of C and can be chosen, for example, to be the lexicographically smallest point of C.

A.3 Random iterated tessellations

A (deterministic) iterated tessellation $\tau = \{C_{n\nu} \cap C_n : \operatorname{int} C_{n\nu} \cap \operatorname{int} C_n \neq \emptyset\}$ in $\mathbb{R}^d$ consists of an initial tessellation $\tau = \{C_n\}_{n\geq 1}$ in $\mathbb{R}^d$ and a sequence $(\tau_n)_{n\geq 1}$ of (embedded) component tessellations $\tau_n = \{C_{n\nu}\}_{\nu\geq 1}$. Hence, in order to define the notion of a random iterated tessellation, we can proceed as follows. Let Ξ be a random convex body in $\mathbb{R}^d$, where $\operatorname{int} \Xi \neq \emptyset$, and let $X = \{\Xi_n\}_{n\geq 1}$ be a random tessellation in $\mathbb{R}^d$. Then, the mapping

$Y(\cdot \mid \Xi) : \Omega \to N(\mathcal{F}')$ defined by $Y(B \mid \Xi) = \sum_{n\geq 1} \delta_{\Xi_n \cap \Xi}(B)\, \mathbb{1}_{\{\text{int } \Xi_n \cap \text{int } \Xi \neq \emptyset\}}$ for $B \in \mathcal{B}(\mathcal{F}')$ is a point process in $\mathcal{C}'$, where $\mathcal{F}' = \mathcal{F} \setminus \{\emptyset\}$. The space of all non-negative and integer-valued measures on $\mathcal{B}(\mathcal{F}')$ is denoted by $N(\mathcal{F}')$, where each $\eta \in N(\mathcal{F}')$ can be represented by a finite or countable sum of Dirac measures δ_F of sets $F \in \mathcal{F}'$, i.e., $\eta(B) = \sum_{n\geq 1} \eta(\{F_n\})\delta_{F_n}(B)$ for any $B \in \mathcal{B}(\mathcal{F}')$, and that $\eta(\{F \in \mathcal{F} : F \cap K \neq \emptyset\}) < \infty$ for any $K \in \mathcal{K}$. Notice that $Y(\cdot \mid \Xi)$ can be seen as one possible way to describe a random tessellation in Ξ.

Furthermore, if $X_0 = \{\Xi_n\}_{n\geq 1}$ is an arbitrary random tessellation in $\mathbb{R}^d$ and if $\{X_n\}_{n\geq 1}$ is an independent sequence of independent and identically distributed random tessellations $X_n = \{\Xi_{n\nu}\}_{\nu\geq 1}$ in $\mathbb{R}^d$, then the mapping $Y : \Omega \to N(\mathcal{F}')$ defined by $Y(B) = \sum_n Y_n(B \mid \Xi_n)$ and $Y_n(B \mid \Xi_n) = \sum_{\nu\geq 1} \delta_{\Xi_{n\nu}\cap\Xi_n}(B)\, \mathbb{1}_{\{\text{int } \Xi_{n\nu}\cap \text{int } \Xi_n \neq \emptyset\}}$ for $B \in \mathcal{B}(\mathcal{F}')$ is called the point-process representation of an iterated random tessellation (or X_0/X_1-nesting) in $\mathbb{R}^d$ with initial tessellation X and component tessellations $X_1, X_2, \ldots$. Clearly, the point process Y is stationary and isotropic, respectively, provided that both the initial tessellation X and the component tessellations $X_1, X_2, \ldots$ possess these properties.

Mean-value relationships can be obtained for iterated tessellations; see e.g. Maier and Schmidt (2003) and the references therein. Consider the case of a 1-fold $X_0/p\,X_1$-nesting ($p \in [0,1]$) and let $\lambda_1, \ldots, \lambda_4$ denote the mean number of vertices, the mean number of edges, the mean number of meshes, and the mean total length of edges per unit area, respectively, with respect to the 1-fold tessellation. Let $\lambda_1^{(0)}, \ldots, \lambda_4^{(0)}$ and $\lambda_1^{(1)}, \ldots, \lambda_4^{(1)}$ denote the corresponding characteristics of X_0 and X_1, respectively. Then,

$$\begin{aligned}
\lambda_1 &= \lambda_1^{(0)} + p\lambda_1^{(1)} + \frac{4p}{\pi}\,\lambda_4^{(0)}\lambda_4^{(1)}\,,\\
\lambda_2 &= \lambda_2^{(0)} + p\lambda_2^{(1)} + \frac{6p}{\pi}\,\lambda_4^{(0)}\lambda_4^{(1)}\,,\\
\lambda_3 &= \lambda_3^{(0)} + p\lambda_3^{(1)} + \frac{2p}{\pi}\,\lambda_4^{(0)}\lambda_4^{(1)}\,,\\
\lambda_4 &= \lambda_4^{(0)} + p\lambda_4^{(1)}\,.
\end{aligned}$$

Table 6 shows the dependence of the four characteristics $\lambda_1, \ldots, \lambda_4$ on p and on the parameters γ_0 and γ_1 of X_0 and X_1, respectively.

Notice that the case of a X_0/X_1-nesting (i.e., $p = 1$) is special in the sense that a symmetry can be observed in the intensities γ_0 and γ_1 of X_0 and X_1, respectively. Therefore, the four

Table 6: Mean-value formulae for X_0/pX_1-tessellations

	PLT/PLT	PLT/PVT	PLT/PDT
λ_1	$\frac{1}{\pi}\,\gamma_0^2 + \frac{1}{\pi}\,p\gamma_1^2 + \frac{4}{\pi}\,p\gamma_0\gamma_1$	$\frac{1}{\pi}\,\gamma_0^2 + 2p\gamma_1 + \frac{8}{\pi}\,p\gamma_0\sqrt{\gamma_1}$	$\frac{1}{\pi}\,\gamma_0^2 + p\gamma_1 + \frac{128}{3\pi^2}\,p\gamma_0\sqrt{\gamma_1}$
λ_2	$\frac{2}{\pi}\,\gamma_0^2 + \frac{2}{\pi}\,p\gamma_1^2 + \frac{6}{\pi}\,p\gamma_0\gamma_1$	$\frac{2}{\pi}\,\gamma_0^2 + 3p\gamma_1 + \frac{12}{\pi}\,p\gamma_0\sqrt{\gamma_1}$	$\frac{2}{\pi}\,\gamma_0^2 + 3p\gamma_1 + \frac{64}{\pi^2}\,p\gamma_0\sqrt{\gamma_1}$
λ_3	$\frac{1}{\pi}\,\gamma_0^2 + \frac{1}{\pi}\,p\gamma_1^2 + \frac{2}{\pi}\,p\gamma_0\gamma_1$	$\frac{1}{\pi}\,\gamma_0^2 + p\gamma_1 + \frac{4}{\pi}\,p\gamma_0\sqrt{\gamma_1}$	$\frac{1}{\pi}\,\gamma_0^2 + 2p\gamma_1 + \frac{64}{3\pi^2}\,p\gamma_0\sqrt{\gamma_1}$
λ_4	$\gamma_0 + p\gamma_1$	$\gamma_0 + 2p\sqrt{\gamma_1}$	$\gamma_0 + \frac{32}{3\pi}\,p\sqrt{\gamma_1}$
	PVT/PLT	PVT/PVT	PVT/PDT
λ_1	$\frac{1}{\pi}\,p\gamma_1^2 + 2\gamma_0 + \frac{8}{\pi}\,p\gamma_1\sqrt{\gamma_0}$	$2(\gamma_0 + p\gamma_1) + \frac{16}{\pi}\,p\sqrt{\gamma_0\gamma_1}$	$2\gamma_0 + p\gamma_1 + \frac{256}{3\pi^2}\,p\sqrt{\gamma_0\gamma_1}$
λ_2	$\frac{2}{\pi}\,p\gamma_1^2 + 3\gamma_0 + \frac{12}{\pi}\,p\gamma_1\sqrt{\gamma_0}$	$3(\gamma_0 + p\gamma_1) + \frac{24}{\pi}\,p\sqrt{\gamma_0\gamma_1}$	$3(\gamma_0 + p\gamma_1) + \frac{128}{\pi^2}\,p\sqrt{\gamma_0\gamma_1}$
λ_3	$\frac{1}{\pi}\,p\gamma_1^2 + \gamma_0 + \frac{4}{\pi}\,p\gamma_1\sqrt{\gamma_0}$	$\gamma_0 + p\gamma_1 + \frac{8}{\pi}\,p\sqrt{\gamma_0\gamma_1}$	$\gamma_0 + 2p\gamma_1 + \frac{128}{3\pi^2}\,p\sqrt{\gamma_0\gamma_1}$
λ_4	$p\gamma_1 + 2\sqrt{\gamma_0}$	$2(\sqrt{\gamma_0} + p\sqrt{\gamma_1})$	$2\sqrt{\gamma_0} + \frac{32}{3\pi}p\sqrt{\gamma_1}$
	PDT/PLT	PDT/PVT	PDT/PDT
λ_1	$\frac{1}{\pi}\,p\gamma_1^2 + \gamma_0 + \frac{128}{3\pi^2}\,p\gamma_1\sqrt{\gamma_0}$	$2p\gamma_1 + \gamma_0 + \frac{256}{3\pi^2}\,p\sqrt{\gamma_1\gamma_0}$	$\gamma_0 + p\gamma_1 + \frac{4096}{9\pi^3}\,p\sqrt{\gamma_0\gamma_1}$
λ_2	$\frac{2}{\pi}\,p\gamma_1^2 + 3\gamma_0 + \frac{64}{\pi^2}\,p\gamma_1\sqrt{\gamma_0}$	$3(p\gamma_1 + \gamma_0) + \frac{128}{\pi^2}\,p\sqrt{\gamma_1\gamma_0}$	$3(\gamma_0 + p\gamma_1) + \frac{2048}{3\pi^3}\,p\sqrt{\gamma_0\gamma_1}$
λ_3	$\frac{1}{\pi}\,p\gamma_1^2 + 2\gamma_0 + \frac{64}{3\pi^2}\,p\gamma_1\sqrt{\gamma_0}$	$p\gamma_1 + 2\gamma_0 + \frac{128}{3\pi^2}\,p\sqrt{\gamma_1\gamma_0}$	$2(\gamma_0 + p\gamma_1) + \frac{2048}{9\pi^3}\,p\sqrt{\gamma_1\gamma_0}$
λ_4	$p\gamma_1 + \frac{32}{3\pi}\,\sqrt{\gamma_0}$	$2p\sqrt{\gamma_1} + \frac{32}{3\pi}\,\sqrt{\gamma_0}$	$\frac{32}{3\pi}\,(\sqrt{\gamma_0} + p\sqrt{\gamma_1})$

characteristics alone cannot be used to discriminate between PVT/PLT and PLT/PVT, between PLT/PDT and PDT/PLT, and between PVT/PDT and PDT/PVT. If $p < 1$ this is not the case.